POLITECNICO DI TORINO
Repository ISTITUZIONALE

Carbon contained mixed matrix membranes based on hydrolyzed polymers of intrinsic microporosity for CO2 separation

Original
Carbon contained mixed matrix membranes based on hydrolyzed polymers of intrinsic microporosity for CO2 separation / Astorino, C., Ferraro, G., Cannone, S.F., Cutaia, L., Lettieri, S., Bartoli, M., Lourenço, M.A.O., Pirri, C.F., Bocchini, S.. - In: SEPARATION AND PURIFICATION TECHNOLOGY. - ISSN 1383-5866. - 424:(2027), pp. 1-14. [10.1016/j.seppur.2026.140717]

Availability:
This version is available at: 11583/3017513 since: 2026-11-04T10:37:08Z

Publisher:
Elsevier

Published
DOI:10.1016/j.seppur.2026.140717

Terms of use:

This article is made available under terms and conditions as specified in the corresponding bibliographic description in the repository

Publisher copyright

(Article begins on next page)

14 November 2026

Separation and Purification Technology 424 (2027) 140717

Contents lists available at ScienceDirect

Separation and Purification Technology

journal homepage: www.elsevier.com/locate/seppur

Carbon contained mixed matrix membranes based on hydrolyzed polymers of intrinsic microporosity for CO_2 separation

Carmela Astorino [a,b,*], Giuseppe Ferraro [a], Salvatore F. Cannone [e], Laura Cutaia [a], Stefania Lettieri [a,*], Mattia Bartoli [b,c], Mirtha A.O. Lourenço [d], Candido Fabrizio Pirri [a,b], Sergio Bocchini [a,b,c]

[a] Department of Applied Science and Technology, Politecnico di Torino, Corso Duca degli Abruzzi 24, Torino, 10129, Italy
[b] Fondazione Istituto Italiano di Tecnologia (CSFT@POLITO), Via Livorno 60, Turin, 10144, Italy
[c] Consorzio Interuniversitario Nazionale per la Scienza e Tecnologia dei Materiali (INSTM), Via G. Giusti 9, Firenze, 50121, Italy
[d] CICECO - Instituto de Materiais de Aveiro, Department of Chemistry, University of Aveiro, Campus Universitário de Santiago, Aveiro, 3810-193, Portugal
[e] Department of Energy, Politecnico di Torino, Corso Duca degli Abruzzi 24, Torino, 10129, Italy

ARTICLE INFO

Editor name: Dr. Philiswa Nomngongo

Keywords:
Nitrogen-doped biochar
Mixed matrix membranes
Polymers of intrinsic microporosity (PIMs)
Gas separation
CO_2 capture
Hydrogen purification

ABSTRACT

Mixed matrix membranes are a promising strategy to overcome the permeability–selectivity trade-off in polymer-based gas separation membranes. In this work, nitrogen-doped biochars derived from chitosan are incorporated at low loadings (1, 2, and 5 wt%) into carboxylated polymers of intrinsic microporosity to fabricate Mixed matrix membranes with enhanced gas separation performance.

Gas sorption–diffusion measurements for CO_2, H_2, CH_4, and N_2 reveal a pronounced, gas-dependent effect of carbon incorporation: relative to the neat caPIM membrane, at 5 wt% filler CO_2 solubility increases, CH_4 solubility decreases, and H_2 solubility remains comparable or slightly lower. In parallel, the diffusivities of CO_2, CH_4, and especially H_2 increase, whereas N_2 diffusivity is markedly reduced, leading to higher CO_2 and H_2 permeabilities combined with strong N_2 rejection over the investigated pressure range.

The combined effects of selective sorption and polymer–filler diffusion result in outstanding separation performance. The membrane containing 5 wt% nitrogen-doped biochar achieves high ideal selectivities, up to ~ 67 for CO_2/N_2 and in the 10^2–10^3 range for H_2/N_2, surpassing Robeson's upper bound for the H_2/N_2 gas pair. These results demonstrate that the biochar acts as a functional, sorption-active phase whose accessible microporosity and surface chemistry cooperatively interact with the caPIM matrix. Overall, nitrogen-doped, bio-derived carbons emerge as intrinsically compatible and selective fillers for high-performance MMMs, offering a sustainable platform for post-combustion CO_2 capture and hydrogen purification from nitrogen-rich gas streams.

1. Introduction

The increasing atmospheric concentration of carbon dioxide (CO_2), largely driven by the extensive use of fossil fuels, represents one of the main contributors to global warming and climate change. Mitigating CO_2 emissions has therefore become an urgent challenge, prompting the development of efficient and scalable separation technologies for post-combustion gas streams. Among the available approaches, polymeric gas separation membranes have emerged as a promising solution due to their low energy demand, modularity and operational simplicity, as extensively discussed by Koros and Fleming, Baker, and Stern. [1–4]

In recent years, growing attention has been devoted to polymers of intrinsic microporosity (PIMs), which combine high permeability with solution processability owing to their rigid and contorted molecular backbones. [5–7] PIM-1, one of the most representative members of this class, has demonstrated exceptional gas permeability and has been shown to approach or exceed Robeson's upper bound for certain gas pairs. [6–8] However, despite its outstanding permeability, pristine PIM-1 exhibits limited selectivity for technologically relevant separations such as CO_2/N_2 and CO_2/CH_4, restricting its direct applicability in carbon capture processes.

To overcome these limitations, several chemical modification strategies have been proposed to enhance CO_2 affinity and selectivity in PIM-based membranes. Functionalization with CO_2-philic groups,

* Corresponding authors at: Department of Applied Science and Technology, Politecnico di Torino, Corso Duca degli Abruzzi 24, 10129 Torino, Italy.
E-mail addresses: carmela.astorino@polito.it (C. Astorino), stefania.lettieri@polito.it (S. Lettieri).

https://doi.org/10.1016/j.seppur.2026.140717
Received 30 April 2026; Received in revised form 7 October 2026; Accepted 7 October 2026
Available online 27 October 2026
1383-5866/© 2026 The Authors. Published by Elsevier B.V. This is an open access article under the CC BY-NC-ND license (http://creativecommons.org/licenses/by-nc-nd/4.0/).

including thioamides, amines and heterocycles, has been explored by Mason et al., Du et al. and others, demonstrating that the introduction of polar functionalities can significantly improve gas separation performance. [9–16] Among these approaches, the introduction of carboxylic acid groups into PIM-1 has proven particularly effective, owing to the strong interactions between –COOH moieties and CO_2 via hydrogen bonding and Lewis acid–base interactions. [17–19]

The base-catalysed hydrolysis of nitrile groups in PIM-1, leading to carboxylated PIMs (caPIMs), has been widely investigated. Satilmis and Budd first highlighted the formation of amide intermediates during hydrolysis, an aspect later clarified and expanded by Santoso et al. and Jeon et al., who reported highly carboxylate-functionalized PIMs exhibiting significantly enhanced CO_2/N_2 selectivity. [20–22] However, these highly functionalized materials were typically obtained through long and energy-intensive hydrolysis processes, often requiring reaction times of several days. Subsequent studies have focused on improving the efficiency of PIM-1 carboxylation while maintaining control over the chemical structure and gas transport properties. [23,24]

More recently, our group has demonstrated that the hydrolysis of PIM-1 can be dramatically accelerated through a microwave-assisted approach, enabling the preparation of highly carboxylated PIMs in only a few hours while preserving excellent gas affinity and separation performance. [25] This advancement provides a robust and scalable route to caPIM materials, making them particularly attractive as membrane matrices for CO_2-selective applications.

Beyond polymer functionalization, an additional strategy to transcend the permeability–selectivity trade-off relies on the development of mixed matrix membranes (MMMs), in which a polymer matrix is combined with a dispersed solid phase. Carbonaceous porous materials are especially appealing as fillers due to their high surface area, chemical stability and strong affinity toward CO_2. [1–7] Indeed, carbonaceous fillers have already been successfully incorporated into several relevant polymer matrices, including activated carbon in Matrimid, heteroatom-doped porous carbon in PIM-1, and biomass-derived biochar in Pebax. [26–28]

Among these, Nitrogen-doped biochars, in particular, have attracted increasing interest as sustainable sorbents derived from biomass waste, as nitrogen functionalities introduce basic sites that enhance CO_2 adsorption and CO_2/N_2 selectivity. [5–7]

Recent reviews on mixed matrix membranes emphasize that the key factor governing MMMs performance is the establishment of a suitable filler–polymer interaction, which enables permeability enhancement while avoiding non-selective transport pathways. Hasan et al. [29] have highlighted that intrinsically compatible fillers, the presence of accessible porosity, and complementary surface chemistry between filler and polymer are crucial to achieve defect-free MMMs capable of surpassing the Robeson upper bound. Within this framework, porous carbonaceous fillers with tailored surface functionality represent a promising class of materials for MMMs design.

While N-doped biochars have been explored as CO_2-selective sorbents and carbonaceous fillers have been incorporated into various polymer matrices, their combination with carboxylated PIM-1 has not yet been investigated. Combining the high intrinsic permeability and CO_2-philic character of caPIM with the selective sorption and transport modulation imparted by N-doped carbon fillers is expected to mitigate the conventional permeability-selectivity tarde-off.

The distinct contribution of this study is therefore the combined materials design and transport analysis: a rapidly hydrolyzed caPIM matrix is paired with low loadings of waste-derived N-doped biochar, and pure-gas solubility, diffusivity, and permeability are resolved for CO_2, N_2, CH_4, and H_2 over 0.2–0.8 bar.

Ideal selectivities and the corresponding Robeson upper bounds are further evaluated for six technologically relevant gas pairs (CO_2/N_2, CO_2/CH_4, H_2/N_2, H_2/CO_2, CH_4/N_2, and H_2/CH_4), providing a comprehensive assessment of the separation performance of the resulting membranes.

In this work, nitrogen-doped biochars were synthesized from chitosan, a nitrogen-containing polysaccharide derived from crustacean shell waste, via microwave-assisted pyrolysis. [3–7]

The nitrogen-doped biochar employed in this work belongs to the same batch previously reported as an efficient CO_2-selective sorbent, extensively characterized in terms of surface chemistry, pore structure, and adsorption behavior by Correia et al. [3]. These biochars were incorporated at low loadings (1, 2 and 5 wt%) into a carboxylated PIM-1 matrix to fabricate mixed matrix membranes.

Gas sorption–diffusion measurements for CO_2, H_2, CH_4 and N_2 reveal that the incorporation of N-doped biochar selectively enhances CO_2 and H_2 transport while strongly suppressing N_2 permeability. In particular, the membrane containing 5 wt% nitrogen-doped biochar achieves high ideal selectivities, up to ~67 for CO_2/N_2, confirming the effectiveness of N-doped biochar as a CO_2-selective filler in caPIM-based MMMs. The same membranes also approach or exceed Robeson's upper bound for H_2/N_2 separation, suggesting potential for hydrogen purification from nitrogen-rich streams.

2. Materials and methods

2.1. Materials

3,3,3,3-Tetramethyl-1,1-spirobiindane-5,5′,6,6′-tetraol (TTSBI, 96%), potassium carbonate (K_2CO_3, ≥98%), *N,N*-dimethylformamide (DMF, ≥99.8%), methanol (MeOH), sodium hydroxide (NaOH, 97%), hydrochloric acid (HCl, 99%), and dimethyl sulfoxide (DMSO, 99.9%) were purchased from Merck-Sigma Aldrich.

2,3,5,6-Tetrafluoroterephthalonitrile (TFTPN, 99%) was obtained from Thermo Fisher Scientific.

All chemicals and solvents were used as received without further purification.

2.2. PIM-1 synthesis

PIM-1 was synthesized following the procedure reported by Budd et al. [9] In a three-necked round-bottom flask, 3,3,3,3-tetramethyl-1,1-spirobiindane-5,5′,6,6′-tetraol (TTSBI, 3.00 g, 0.008813 mol) and 2,3,5,6-tetrafluoroterephthalonitrile (TFTPN, 1.76 g, 0.008813 mol) were dissolved in dry *N,N*-dimethylformamide (DMF, 60 mL). Anhydrous potassium carbonate (K_2CO_3, 5.53 g, 0.040 mol) was then added, and the reaction mixture was stirred at 65 °C for 72 h under a nitrogen atmosphere.

After completion of the reaction, the mixture was poured into 400 mL of deionized water to precipitate the polymer. The resulting solid was collected by centrifugation, washed twice with deionized water and several times with methanol to remove residual salts and solvent, and subsequently dried under vacuum at 40 °C until constant weight. PIM-1 was obtained as a yellow powder with a yield of 91%.

2.3. PIM-1 hydrolysis

The hydrolysis of PIM-1 was carried out following the procedure originally reported by Jeon al. [8], with modifications introduced by our group through the use of microwave-assisted heating.

Sodium hydroxide (NaOH, 6.4 g, 0.16 mol) was dissolved in 40 mL of a 1:1 (*w*/w) mixture of deionized water and ethanol. PIM-1 powder (2.5 g) was then added to the alkaline solution, and the resulting suspension was transferred to a microwave reactor equipped with magnetic stirring (Milestone S.r.l., Start Synth). The reaction mixture was heated under microwave irradiation with a maximum power of 800 W until a temperature of 150 °C was reached and subsequently maintained at this temperature under continuous stirring for 1 h.

After completion of the microwave treatment, the reaction mixture was allowed to cool to room temperature and was gradually neutralized with concentrated hydrochloric acid until pH 4. The suspension was

then stirred overnight at room temperature to ensure complete precipitation of the hydrolyzed polymer. The resulting solid was collected by filtration, washed several times with methanol to remove residual salts and impurities, and finally dried under vacuum at 100 °C until constant weight.

In the present study, only caPIM synthesized with a one-hour reaction time was employed; therefore, it will be referred to simply as caPIM throughout the text. For the batch investigated here, the extent of nitrile conversion is assessed qualitatively from vibrational spectroscopy; a validated numerical degree of carboxylation and post-hydrolysis molecular-weight distribution were not available.

2.4. Synthesis of biochar

The carbon adsorbent used in this work is the chitosan-derived biochar CTOP600MW, prepared by microwave-assisted pyrolysis as described in Correia et al. [3]., and kindly provided by the authors. In the original study, this material was reported to have a BET surface area of 307 $m^2\ g^{-1}$, a pore volume of 0.139 $cm^3\ g^{-1}$, and a predominantly ultramicroporous pore size distribution in the 0.34–0.70 nm range.

Nitrogen-doped biochar was prepared by microwave-assisted pyrolysis of commercial chitosan (medium molecular weight, degree of deacetylation 75–85%, low viscosity 200–800 cps for a 1 wt% solution in acetic acid; Sigma-Aldrich). Typically, 1.5 g of chitosan powder was placed in a ceramic crucible and introduced into a Phoenix™ microwave muffle furnace.

Pyrolysis was carried out under a continuous nitrogen flow according to the following heating program: (i) heating at 5 °C min^{-1} to 200 °C and holding for 5 min, followed by (ii) heating at 5 °C min^{-1} to 600 °C and holding for 20 min. After completion of the thermal treatment, the sample was cooled to room temperature under nitrogen atmosphere, yielding the nitrogen-doped biochar (CTOP600_MW) with a mass yield of 31.6%. [3]

2.5. Preparation of caPIM based membranes

Membranes were prepared by solvent casting. Briefly, 200 mg of caPIM were dissolved in 3 mL of *N*-methyl-2-pyrrolidone (NMP) at 80 °C under continuous stirring until a homogeneous solution was obtained. The solution was then cast onto a low-density polyethylene (LDPE) substrate placed on a heated plate maintained at 80–120 °C to promote partial solvent evaporation.

The membrane–substrate assembly was subsequently transferred to a vacuum oven and kept at 40 °C for 2 h to allow gradual membrane detachment from the substrate and to prevent fracture formation associated with rapid solvent removal. Finally, the membranes were dried under vacuum at 100 °C for 16 h to ensure complete removal of residual solvent.

2.6. Preparation of caPIM with carbons-based membranes

For the preparation of caPIM/carbon-based mixed matrix membranes, 160 mg of caPIM powder were dissolved in 3 mL of *N*-methyl-2-pyrrolidone (NMP) at 80 °C under stirring until complete dissolution. In a separate vial, the appropriate amount of carbon filler was dispersed in 1 mL of the same solvent.

The carbon dispersion was then combined with the polymer solution, and the resulting mixture was stirred to ensure homogeneous distribution of the filler. The composite solution was subsequently processed following the same solvent-casting and drying procedure described for the neat caPIM membranes. The resulting membranes with different carbon loadings (1, 2, and 5 wt%) are schematically illustrated in Fig. 1. The membrane with 5 wt% represents the highest loading that still yields mechanically robust membranes.

2.7. Characterizations procedures

Thermogravimetric analysis coupled with infrared spectroscopy (TGA–IR) was performed using a NETZSCH TG 209 F1 thermogravimetric analyzer coupled via a transfer line maintained at 230 °C to a Bruker TENSOR II FTIR spectrometer. The IR gas cell was kept at 200 °C. Approximately 3 mg of sample were placed in alumina crucibles and heated from 30 °C to 800 °C at a constant heating rate of 20 K min^{-1} under a nitrogen flow of 40 mL min^{-1}. Prior to analysis, samples were subjected to three vacuum cycles to remove residual solvent. The experimental uncertainty in weight measurements was ±1%. FTIR spectra of the evolved gases were collected in absorbance mode over the range 500–4000 cm^{-1}.

FTIR spectra of PIM-1 and hydrolyzed derivatives were acquired in transmission mode using KBr pellets with a Bruker TENSOR II spectrophotometer. Peak assignments were performed according to Lin-Vien et al. [12].

Surface morphology of the membranes was investigated using a Zeiss Supra™ 25 field-emission scanning electron microscopes (FESEM) operated at an accelerating voltage of 5 kV. Images were collected under high-vacuum conditions using a secondary electron detector. Samples were mounted on aluminum stubs using conductive carbon tape and, when necessary, sputter-coated with a thin gold layer to minimize charging effects.

Raman spectra were recorded using a Renishaw inVia Raman microscope equipped with a 785 nm excitation laser (output power 0.5 mW). Spectra were collected with an integration time of 10 s and averaged over three accumulations to improve the signal-to-noise ratio. Instrument calibration was performed using the characteristic silicon band at 516 cm^{-1}.

Pure-gas adsorption–desorption isotherms were measured using a Dynamic Vapor Sorption (DVS) instrument (Surface Measurement

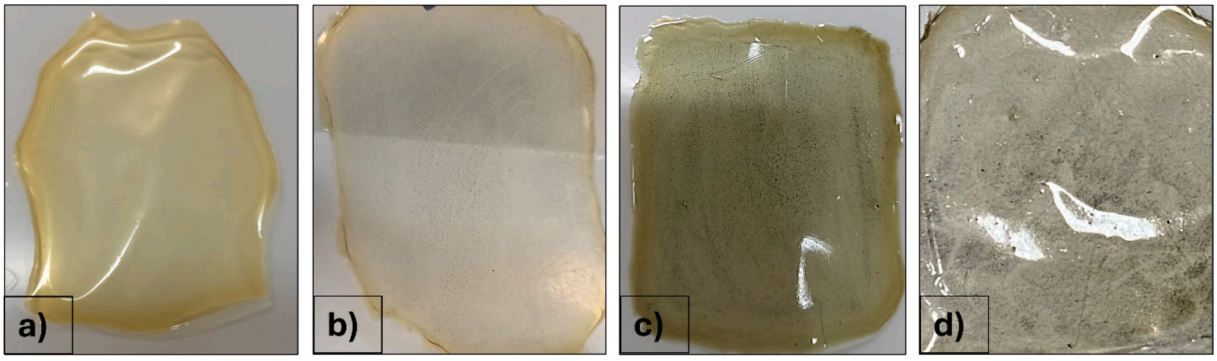


Fig. 1. Photographs of caPIM-based membranes prepared by solvent casting from *N*-methyl-2-pyrrolidone (NMP) onto a low-density polyethylene (LDPE) support: (a) neat caPIM membrane; (b) caPIM membrane containing 1 wt% carbon filler; (c) caPIM membrane containing 2 wt% carbon filler; (d) caPIM membrane containing 5 wt% carbon filler.

Systems). Samples were degassed at 80 °C until the mass-change rate (dm% dt^{-1}) fell below 0.001% min^{-1}, ensuring complete removal of volatile species. Gas pressure increased stepwise from 0.2 to 0.8 bar in increments of 0.2 bar. At each pressure step, equilibrium was reached when the mass-change rate again dropped below 0.001% min^{-1}. Between successive adsorption steps, desorption under vacuum was applied. Equilibrium mass values were recorded at each pressure.

All permeation measurements were performed at 40 °C using pure CH_4, CO_2, H_2, and N_2 at a partial pressure of 1 bar under constant flow conditions.

Measurements were performed with single gases due to the lack of a system for preparing and controlling gas mixtures at the time of the experiments.

Buoyancy effects arising from the surrounding gas atmosphere were corrected by independently determining the sample volume and density. The gas density in the DVS chamber was estimated to be assuming ideal-gas behavior, using the gas molecular weight, instantaneous pressure P (t), and chamber temperature T(t). The apparent buoyancy-related mass variation m_B(t) was calculated and applied to the raw DVS signal of the membrane, while being subtracted from a blank experiment conducted under identical pressure–temperature conditions. The corrected signal was used to determine the net absorbed gas mass.

$$\rho_g(t) = \frac{M_w p(t)}{R[T(t) + 273.15]}$$

$$m_B(t) = \rho_g(t) V_m$$

$$m_{abs(t)} = m_{raw}^{mem}(t) + m_B(t) - m_{raw}^{blank}(t)$$

The absorbed gas moles were computed as $n(t) = \frac{m_{abs}(t)}{M_w}$ and normalised by the total membrane area A to obtain the molar uptake per unit area. For each pressure step, the equilibrium uptake M_∞ was identified as the plateau value of M_t^{exp}, l is the membrane half-thickness.

$$M_t^{exp} = n(t)/A$$

Once the target pressure of a given step is reached, the actual pressure $P(t)$ becomes approximately constant. The post-ramp part of the uptake curve was analyzed assuming diffusion in a plane sheet of thickness $2l$ suddenly exposed to a constant surface concentration c_s. In this case the normalised uptake follows the classical Crank solution

$$\frac{M_t}{M_\infty} = 1 - \frac{8}{\pi^2} \sum_{n=0}^{\infty} \frac{1}{(2n+1)^2} \exp\left(\frac{-(2n+1)^2 \pi^2 D_{st} t}{4l^2}\right)$$

where D_{st} is the diffusivity corresponding to the constant-pressure regime ("stable" diffusivity).

For each pressure step, the time at which the pressure reached a stable plateau was automatically detected from the pressure trace $p(t)$ (threshold on both relative difference from the target pressure and local slope dp/dt). Only data points after this stabilization time were used in a non-linear least-squares fit of the above equation to the experimental normalised uptake M_t^{exp}/M_∞. The fitting parameter is D_{st}, while l and M_∞ are fixed by the membrane geometry and the equilibrium uptake. This yields a constant pressure diffusivity for each pressure level.

During the pressurization ramp, the upstream gas pressure does not change instantaneously but increases approximately linearly from the previous equilibrium value to the new target pressure over a finite time interval, during which most of the transient gas uptake occurs. The uptake of a plane sheet subjected to a time-dependent boundary concentration can be described by extending the classical Crank solution for diffusion in a plane sheet to the case of a linear pressure ramp [30].

The resulting analytical expression for the molar uptake was evaluated assuming a linearly increasing surface concentration, yielding a diffusivity value, D_{ramp}, specifically associated with the finite pressurization ramp

$$M_t^{mod,ramp}(D_{ramp}) = \frac{k_\Phi l^3}{D_{ramp}} \left[\frac{2D_{ramp} t}{l^2} - \frac{2}{3} + \frac{64}{\pi^4} \sum_{n=0}^{\infty} \frac{\exp\left(\frac{-(2n+1)^2 \pi^2 D_{st} t}{4l^2}\right)}{(2n+1)^4}\right]$$

For each pressure step, the experimental ramp segment was selected from the pressure trace, and the corresponding experimental uptake M_t^{exp} was converted to mol cm^{-2} as described above. The coefficient k_p was obtained by linear regression of $p(t)$ in this interval, and k_ϕ was then calculated using the solubility determined at that pressure. The ramp diffusivity D_{ramp} was finally identified by minimising the sum of squared residuals between experimental and modelled uptake.

$$\min(D_{ramp}) \sum_{t\ \epsilon\ ramp} \left[M_t^{ramp} - M_t^{mod,ramp}(D_{ramp})\right]^2$$

For each pressure step, the DVS data thus provide an experimental uptake curve $M_t^{exp}(t)$ in mol cm^{-2}, which is compared with two model predictions:

- $M_t^{mod,ramp}(t; D_{ramp})$, obtained using the Crank-based solution with a linearly increasing upstream concentration, fitted on the pressure-ramp segment.
- $M_t^{mod,st}(t; D_{st})$, obtained using the classical Crank step-change solution with constant upstream concentration, fitted on the post-ramp, constant-pressure segment.

Both models use the same experimentally determined solubility S and membrane half-thickness l, differing only in the value of the diffusivity (ramp vs. constant-pressure). The quality of the fits and the internal consistency of the analysis are assessed by visually comparing $M_t^{exp}(t)$ with $M_t^{mod,ramp}(t)$ and $M_t^{mod,st}(t)$ for each pressure step, and by computing statistical indicators (e.g. coefficient of determination R^2 and root-mean-square error). These comparisons provide a direct link between the raw microbalance signal and the transport parameters S, D_{ramp} and D_{st}, which are subsequently used to derive the pure-gas permeability reported in Barrer and ideal pair selectivities.

For each gas and pressure, the reported solubility, diffusivity, and permeability values were calculated as mean values from independent replicate measurements.

The associated uncertainty was evaluated as the standard error of the mean of the replicate tests performed at the same pressure, according to $u = [\Sigma(x_i - \bar{x})^2/(n-1)]^{1/2} / \sqrt{n}$, where x_i is the value obtained from each individual test, $\bar{x}$ is the average value, and n is the number of replicate tests. A minimum of three tests was considered for each gas.

Permeability coefficients were calculated as the product of the solubility and diffusion coefficients ($P = S \cdot D$), and the corresponding uncertainty was obtained by propagating the standard errors of S and D as $u_P = P \cdot [(u_S/S)^2 + (u_D/D)^2]^{1/2}$, where u_S and u_D are the standard errors of the solubility and diffusion coefficients, respectively.

As a consequence of this propagation, gases characterized by very low solubility in the membrane exhibit larger relative uncertainties in permeability. In these cases the net mass uptake measured by the microbalance approaches the sensitivity limit of the instrument, so that the relative standard error of the solubility term (u_S/S) increases and, upon propagation, results in a larger relative uncertainty in permeability. Accordingly, the largest error bars reported for some gas pairs (in particular those involving the least soluble gases, such as N_2) do not reflect poor repeatability of the membrane tests, but rather the intrinsic sensitivity limit of the gravimetric method when the absorbed amount is very small.

3. Results and discussion

All the structural and morphological characterizations of the MMMs

and of the composite systems are discussed below. The characterization data for the carbonaceous fillers alone (XRD, Raman, FE-SEM and EDS) are provided in the Supporting Information (Supplementary Figs. S5–S8).

3.1. Characterization of mixed matrix membranes

3.1.1. Fourier transform infrared spectroscopy (FTIR)

The FTIR spectra of caPIM-based membranes are shown in Fig. 2. The characteristic absorption bands of caPIM are clearly observed. [14]

The spectral region between 1000 and 1800 cm^{-1} is mainly associated with aromatic C═C stretching vibrations and amide-related functional groups. [31] In particular, the amide carbonyl stretching vibration ($\nu_{(C=O)}$) is detected at 1678 cm^{-1}, [31] while the $\nu_{(N-H)}$ stretching modes appear in the range 3000–3400 cm^{-1}. [21] A comparison between the spectra of pristine PIM-1 and caPIM (Fig. S10, Supporting Information) further shows the disappearance of the nitrile stretching band at 2245 cm^{-1}, together with the appearance of the amide-related bands described above, consistent with the conversion of nitrile groups into amide/carboxyl functionalities during hydrolysis. [8]

The relatively strong intensity of these absorption bands indicates a significant presence of amide functionalities within the caPIM structure. The incorporation of carbon fillers at loadings of 1, 2, and 5 wt% does not lead to appreciable changes in the FTIR spectra. No new absorption bands, peak shifts, or significant variations in band intensities are observed upon filler addition, indicating that the primary chemical structure of caPIM is preserved in the mixed matrix membranes. This suggests that the carbon fillers do not induce chemical modifications or strong specific interactions detectable by FTIR within the polymer matrix.

3.1.2. Thermal stability and degradation behavior (TGA–IR)

Thermogravimetric analysis (TGA) was performed on all membranes to assess their thermal stability and to evaluate the effect of carbon filler incorporation. The comparative TGA curves are reported in Fig. 3. All samples exhibit a similar overall degradation profile, indicating that the presence of carbon fillers does not significantly alter the thermal decomposition pathway of the caPIM matrix.

As shown in Fig. 3, two initial weight losses are observed at approximately 190 °C and 246 °C for all membranes. These events are attributed to the presence of residual *N*-methyl-2-pyrrolidone (NMP) and to the release of CO_2. This assignment is supported by the TGA–IR analysis of the evolved gases (Supporting Information, Figs. S1 and S2),

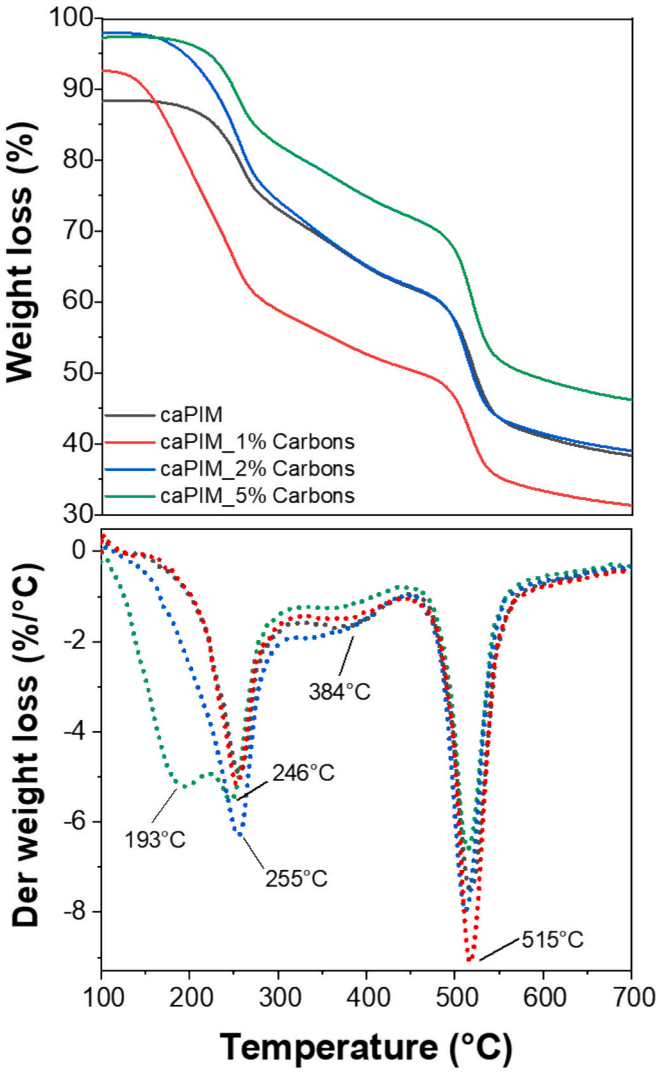


Fig. 3. Thermogravimetric curves of neat caPIM and caPIM-based membranes containing different carbon loadings.

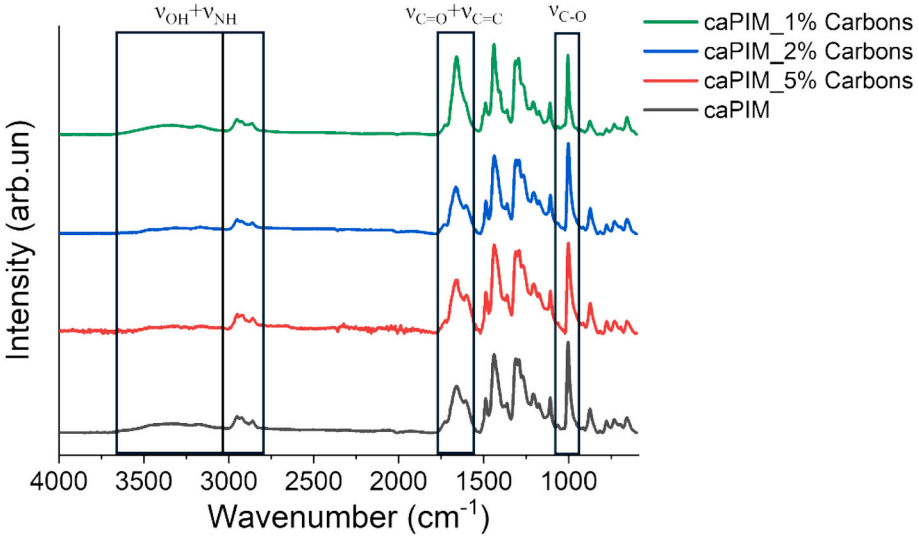


Fig. 2. FTIR spectra of neat caPIM and caPIM membranes containing carbon fillers.

where characteristic absorption bands of NMP and CO_2 are clearly detected. In particular, the caPIM membrane containing 5 wt% carbon exhibits a more pronounced shoulder around 190 °C, suggesting a higher amount of retained NMP compared to the other samples.

The IR spectrum associated with the weight loss at ~190 °C (Fig. S1) displays characteristic bands of NMP, including a weak and broad absorption in the 2800–3000 cm^{-1} range, a peak at 1700 cm^{-1}, and multiple signals between 1100 and 1500 cm^{-1}. [17] The presence of CO_2 is confirmed by the absorption band at approximately 2200 cm^{-1}. [18] The subsequent weight loss at ~246 °C is accompanied by a more intense evolution of CO_2, as evidenced by the corresponding IR spectrum (Fig. S2), which is consistent with a decarboxylation process. [8] Typical CO_2 absorption features are observed at 2350 cm^{-1}, between 3600 and 3700 cm^{-1}, and around 700 cm^{-1}.

A further degradation occurring around 380 °C is attributed to the decomposition of amide functionalities present in the caPIM structure. This interpretation is supported by the TGA–IR analysis of the evolved gases (Fig. S3), which shows absorption bands at approximately 3400 cm^{-1} and 900 cm^{-1}, characteristic of NH_3. In this temperature range, the amide C═O signal overlaps with the carbonyl band of the NMP lactam, resulting in a higher overall signal intensity compared to the lower-temperature events.

The main-chain degradation of caPIM occurs at higher temperatures, with a major weight loss centered around 515 °C. The corresponding TGA–IR spectrum (Fig. S4) reveals the evolution of CO_2 (~2350 cm^{-1}), CO (~2100 cm^{-1}), and H_2O (~3600 cm^{-1}), consistent with the degradation of the dioxane moieties and the polymer backbone. The concurrent release of methane and ammonia further indicates the progressive decomposition of the remaining polymer structure. [8]

Carbon loading affects the residual mass more than the main degradation temperature. At 700 °C, the remaining mass is approximately 38% for neat caPIM, 31% for the 1 wt% membrane, 39% for the 2 wt% membrane, and 46% for the 5 wt% membrane. The non-monotonic response at 0–2 wt% shows that low filler contents do not produce a systematic thermal-stabilization effect. The larger residue at 5 wt% is consistent with a greater char-forming contribution, although its magnitude cannot be assigned to filler alone because this sample also retains more NMP and undergoes a larger low-temperature mass loss. Accordingly, the data support similar backbone thermal stability across the series and an increased high-temperature residue only at the highest loading.

3.1.3. *Field Emission Scanning Electron Microscopy (FESEM)*

The morphology of the neat caPIM membrane and caPIM membranes containing 1, 2, and 5 wt% of carbon filler was investigated by field-emission scanning electron microscopy (FESEM). Representative cross-sectional views (scale bar 20 µm) and their corresponding high-magnification micrographs (scale bar 1 µm) are displayed in Fig. 4. For completeness, FESEM micrographs and EDS analysis of the isolated chitosan-derived carbon materials are reported in the Supporting Information (Figs. S5 and S6).

The neat caPIM membrane exhibits a distinct cross-sectional fractured surface characterized by a highly structured and rough morphology (Fig. 4a,b). This open framework is consistent with solvent-cast films of rigid and polar PIM derivatives, reflecting the combined effects of strong polymer–solvent interactions, limited chain mobility, and solvent evaporation dynamics during film solidification.

Upon incorporation of carbon fillers, the microstructure evolves systematically. At lower filler loadings (1 and 2 wt%, Figs. 4e–h), the fracture surface appears smoother than that of the neat caPIM membrane, possibly reflecting altered fracture or solvent-evaporation behavior in the presence of dispersed particles. As evidenced by FESEM of the pristine carbon (Figs. S5–S6), the lamellar particles (~200–300 µm) undergo substantial fragmentation during film casting, yielding submicrometric domains that are uniformly embedded within the polymer matrix [32].

The isolated chitosan-derived carbon exhibits a BET specific surface area of 307 $m^2\ g^{-1}$ and a total pore volume of 0.139 $cm^3\ g^{-1}$, together with an ultramicropore-size distribution centred in the 0.34–0.70 nm range.[3] These textural properties are potentially relevant to gas sorption and transport; however, because they were measured on the pristine biochar, the fraction of the original porosity that remains accessible after fragmentation and incorporation into caPIM cannot be determined from the present data.

At the highest loading (5 wt%, Figs. 4c,d), the cross-sections display localized roughness and irregularities that correlate with the macroscopic heterogeneity observed in the membrane photographs (Fig. 1). Such localized aggregates are commonly reported in carbon-filled matrices and can arise from strong filler–filler cohesive interactions (Van der Waals and, for graphitic domains, π–π contacts) [33]. Notably, across all investigated loadings, the polymer phase appears to wet and encapsulate the carbon domains effectively: no interfacial cracks or voids are detected at the filler–polymer boundary within the resolution of our measurements, indicating satisfactory adhesion and structural integrity under the tested conditions [34].

At 5 wt% filler loading, localized heterogeneity and filler-rich regions are observed, indicating that this composition approaches the upper practical limit for filler incorporation in the present caPIM matrix. However, this observed heterogeneity does not necessarily lead to non-selective transport pathways, as the polymer phase effectively encapsulates the carbon domains. Accordingly, the 5 wt% membrane should be regarded as a functional mixed matrix membrane with local

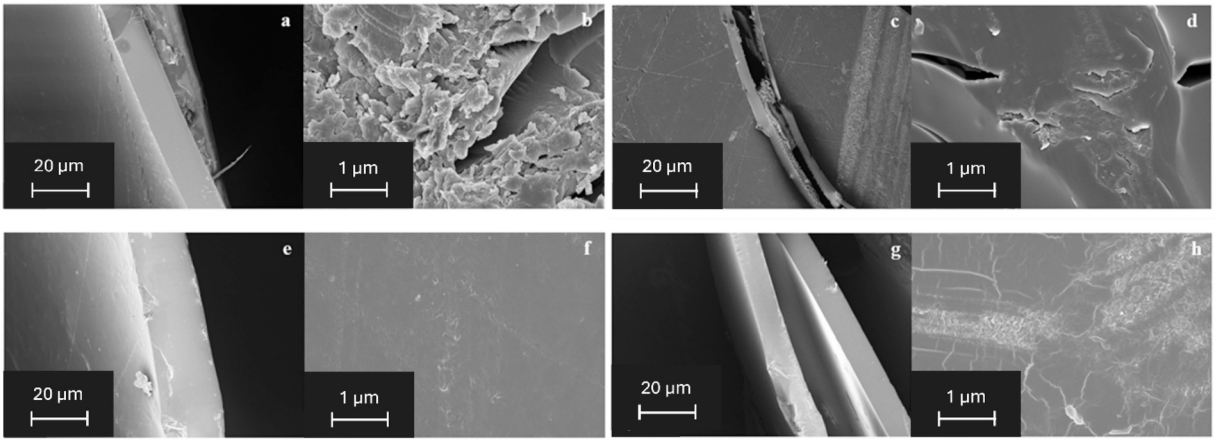


Fig. 4. FESEM images of neat caPIM membrane (a,b); caPIM membrane containing 5 wt% carbon filler (c,d); caPIM membrane containing 2 wt% carbon filler (e,f); caPIM membrane containing 1 wt% carbon filler (g,h).

morphological heterogeneity rather than as a fully homogeneous polymer–filler mixture.

3.1.4. Raman spectroscopy

The Raman spectrum of the chitosan-derived carbon material is reported in the Supporting Information (Fig. S7). Two characteristic bands are observed at approximately 1350 and 1580 cm^{-1}, corresponding to the D and G bands, respectively. [20] The D band is associated with disordered carbon structures, while the G band arises from the in-plane stretching vibrations of sp^2-bonded carbon atoms in graphitic domains.

Deconvolution and integration of the D and G bands yield an intensity ratio (I_G/I_D) of 3.34 for the chitosan-derived carbons. The corresponding crystallite size, estimated from the Raman analysis, is 27.29 nm, indicating a relatively high degree of graphitization with extended sp^2 domains and a low defect density. [35]

Fig. 5 compares the Raman spectra of neat caPIM membranes and caPIM membranes containing different carbon loadings. In the mixed matrix membranes, the spectral region typically associated with the D and G bands of carbon is largely dominated by the intrinsic vibrational modes of the caPIM matrix. [36] In particular, the band observed around 1580 cm^{-1} is primarily attributed to the stretching vibrations of aromatic C═C bonds within the polymer backbone, which overlap with the G band commonly assigned to graphitic carbon. [21] As a result, the direct contribution of the carbon filler to the Raman response of the mixed matrix membranes is partially masked by the polymer matrix.

Additional vibrational features are observed in the region between approximately 1650 and 1700 cm^{-1}, corresponding to the stretching modes of C═O and N—H bonds associated with amide functionalities. The spectral region between 1000 and 1300 cm^{-1} is dominated by bands attributed to C–O–C stretching vibrations, confirming the presence of ether linkages in the caPIM structure. [22]

Any Raman signals are detected in the region associated with the C≡N stretching vibration (≈2220–2260 cm^{-1}) supporting the hydrolysis of the nitrile groups originally present in PIM-1 and supporting the successful conversion to the amide-functionalized caPIM structure. [23]

The XRD pattern of the chitosan-derived carbon is reported in the Supporting Information (Fig. S8), and is consistent with the disordered, predominantly amorphous structure indicated by the Raman analysis.

3.2. Gas separation performance

All measurements were performed under single-gas conditions using a DVS-based constant-volume setup. The tests required long experimental runs and were repeated over time intervals exceeding one week for each sample; no systematic drift in performance was observed, indicating stable membrane behavior over at least several days under the tested conditions.

3.2.1. Dynamic vapor sorption Instrument (DVS)

3.2.1.1. Gas solubility. The solubility coefficients of CH_4, H_2, N_2, and CO_2 in caPIM and in caPIM-based mixed matrix membranes containing different carbon loadings are reported as a function of gas partial pressure in Fig. 6.

For CO_2, carbon incorporation has a clear and systematic effect that becomes significant at the highest filler loading. In pristine caPIM, CO_2 solubility decreases moderately with pressure, from 0.16 cm^3(STP)/(cm^3·cmHg) at 0.2 bar to 0.12 cm^3(STP)/(cm^3·cmHg) at 0.8 bar. The addition of 1 wt% and 2 wt% carbon leads to slightly lower CO_2 solubility compared to the neat polymer over the whole pressure range. In contrast, membranes containing 5 wt% carbon consistently exhibit enhanced CO_2 uptake. At 0.2 bar, caPIM_5% reaches 0.21 cm^3(STP)/(cm^3·cmHg), corresponding to an increase of approximately 30% with respect to caPIM, while a smaller but persistent positive offset is maintained up to 0.8 bar.

This behavior is consistent with the intrinsic sorption properties of the chitosan-derived, N-doped biochar employed as filler, which has been shown to display a strong affinity toward CO_2 and a pore structure dominated by ultramicropores in the 0.3–0.4 nm range. When present at sufficiently high loading, the carbon phase can thus introduce additional CO_2-selective sorption sites and locally modify the free-volume

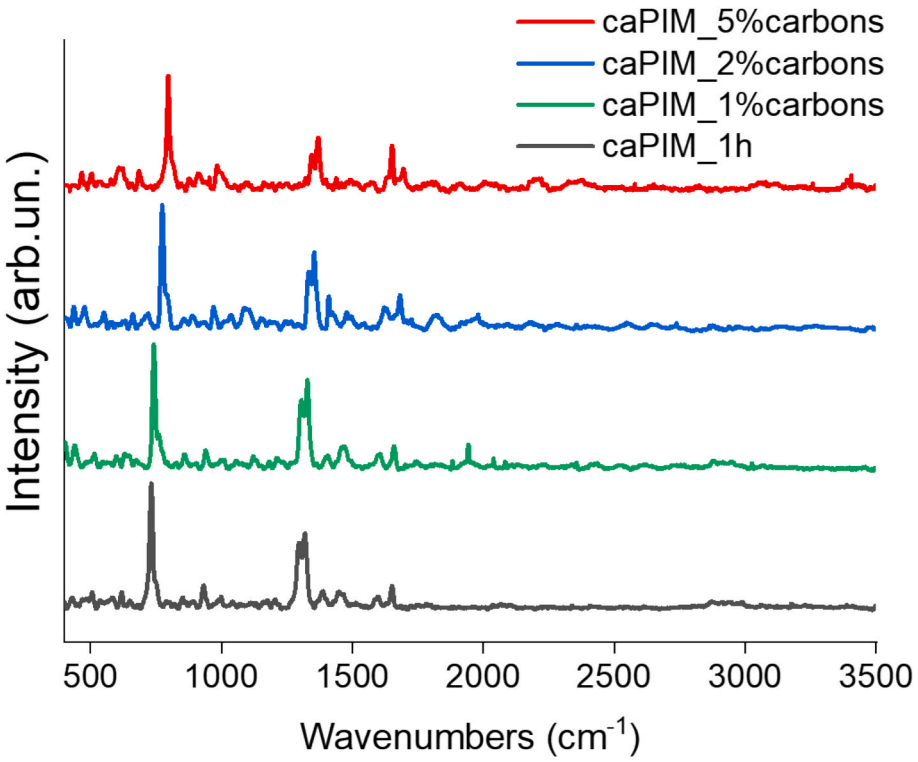


Fig. 5. Raman spectra of caPIM and caPIM + carbons membranes in the range of 3500–400 cm^{-1}.

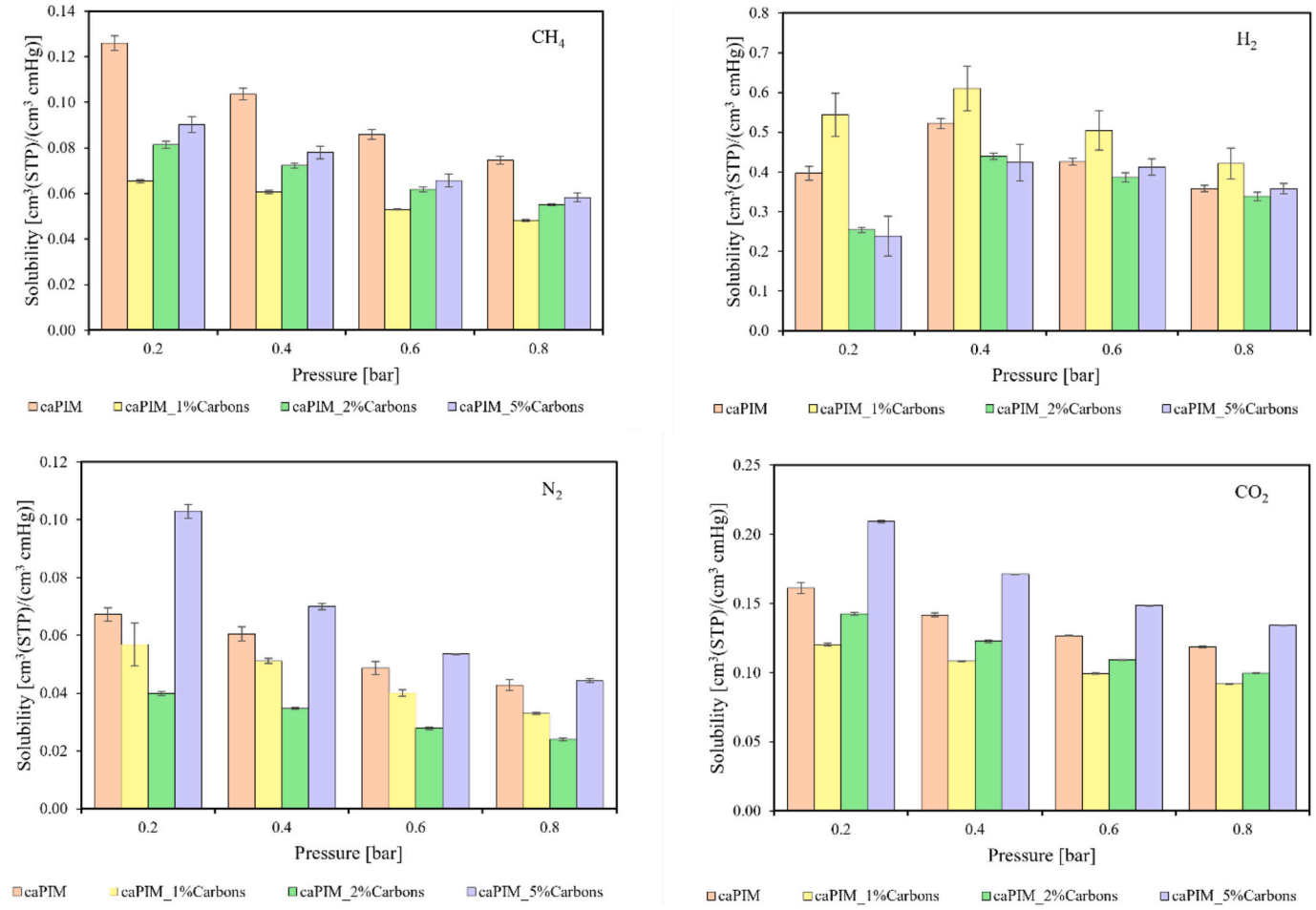


Fig. 6. Solubility coefficients of CH_4, H_2, N_2, and CO_2 in caPIM and caPIM-based mixed matrix membranes containing 1, 2, and 5 wt% carbon filler, plotted as a function of gas partial pressure. Error bars represent the standard error calculated from replicate measurements performed at the same pressure.

landscape of the polymer matrix. At lower loadings, the amount of carbon is likely insufficient to significantly perturb the overall sorption environment of caPIM, resulting in solubility values comparable to or slightly lower than those of the neat polymer.

A more nuanced trend is observed for N_2. In caPIM, N_2 solubility is low and slightly decreases with pressure. The incorporation of 1 wt% and 2 wt% carbon further reduces N_2 solubility, particularly at intermediate and high pressures. In contrast, the membrane containing 5 wt% carbon shows a modest increase in N_2 solubility at low pressure, while values at higher pressures converge toward those of the pristine caPIM polymer. This behavior reflects the weak affinity of the carbon filler toward N_2, combined with competing effects of additional sorption sites and changes in polymer packing at higher filler loading.

Methane solubility is higher than that of N_2 but remains significantly lower than that of CO_2. In pristine caPIM, CH_4 solubility decreases from 0.13 cm^3(STP)/(cm^3·cmHg) at 0.2 bar to 0.07 cm^3(STP)/(cm^3·cmHg) at 0.8 bar. Carbon-containing membranes exhibit comparable or systematically lower CH_4 solubilities, particularly at low and intermediate loadings. Even at 5 wt%, CH_4 solubility does not exceed that of caPIM, indicating that the carbon filler does not introduce favorable sorption sites for methane and may partially replace or block polymer regions that contribute to CH_4 uptake. This trend is in line with the low CH_4 affinity reported for the chitosan-derived biochar used in this work.

Hydrogen displays the highest solubility among the non-condensable gases. In caPIM, H_2 solubility increases at low pressure and then decreases at 0.8 bar. Carbon-loaded membranes exhibit a loading-dependent response: the 1 wt% formulation shows systematically higher H_2 solubility than caPIM over the entire pressure range, whereas the 2 wt% and 5 wt% membranes display values comparable to or slightly lower than those of the neat polymer, converging within experimental uncertainty at high pressure. This suggests that low carbon loadings can enhance local H_2 affinity, while higher loadings mainly affect gas transport through changes in diffusivity rather than sorption.

Overall, the solubility data demonstrate that carbon incorporation modulates gas–polymer interactions in a strongly gas-dependent manner. In particular, the membrane containing 5 wt% carbon combines enhanced CO_2 sorption with unchanged or reduced solubility for N_2, CH_4, and H_2, reflecting the intrinsic selectivity of the N-doped biochar toward CO_2. This selective modulation of sorption constitutes the first contribution of the carbon filler to the improved separation performance of caPIM-based mixed matrix membranes. This behavior is fully consistent with the mechanisms described for effective MMMs, where fillers with intrinsic adsorption selectivity and good polymer compatibility can translate their sorption properties into membrane-level performance. [29]

The inclusion of pristine PIM-1 as a reference provides further insight into the effect of hydrolysis and carbon incorporation on gas sorption (Table S1). Pristine PIM-1 displays the highest CO_2 solubility among the investigated membranes, decreasing from approximately 0.32 cm^3(STP)/(cm^3·cmHg) at 0.2 bar to 0.24 cm^3(STP)/(cm^3·cmHg) at 0.8 bar. These values are higher than those measured for caPIM_5% carbons, which range from 0.21 to 0.13 cm^3(STP)/(cm^3·cmHg) over the same pressure interval. However, for the other gases, PIM-1 exhibits lower or comparable solubility compared with the caPIM-based membranes. In particular, H_2 and N_2 solubilities in pristine PIM-1 are markedly lower than those observed for caPIM and caPIM/carbon

membranes.

This comparison indicates that the hydrolysis of PIM-1 and the subsequent incorporation of carbon fillers substantially modify the gas sorption environment. While pristine PIM-1 retains a high CO_2 uptake, the caPIM/carbon system provides a more selective sorption–diffusion balance, especially when combined with the strong suppression of N_2 transport observed in the diffusivity and permeability data.

3.2.1.2. Gas diffusivity. Diffusivity coefficients derived from DVS measurements are reported in Fig. 7 as a function of gas partial pressure for caPIM and caPIM-based mixed matrix membranes containing different carbon loadings.

The measured diffusivities reflect the effective membrane and cannot uniquely separate transport through the polymer, the biochar, and the interface. A useful matrix-level reference is that hydrolysis of PIM-1 has been associated with reduced chain spacing and a redistribution toward smaller free-volume elements, which lowers segmental transport. [37] Filler addition may then introduce competing effects: accessible ultramicropores or interfacial free volume can shorten local pathways, whereas particle-induced tortuosity or local packing changes can hinder transport. The present D data are interpreted within this framework, while noting that neither Tg, DMA, nor in-membrane free volume was measured.

For CO_2, caPIM diffusivities are on the order of $10^{-9}\,cm^2\,s^{-1}$ and decrease moderately with pressure. At 0.4 bar, D increases from approximately $4.1 \times 10^{-9}\,cm^2\,s^{-1}$ in caPIM to 7.7×10^{-9} and $6.7 \times 10^{-9}\,cm^2\,s^{-1}$ at 1 and 2 wt% biochar, respectively. This trend is consistent with an additional interfacial and/or porous contribution, but it does not establish a continuous carbon pathway. The smaller gain at 5 wt% indicates that the competing effects of heterogeneity and tortuosity become more important at the highest loading.

CH_4 diffusivity also increases after biochar addition, although CH_4 solubility does not. The permeability gain for CH_4 is therefore diffusion-controlled. The result is consistent with altered pathway connectivity or interfacial free volume, but the current data do not distinguish these possibilities from partial access to the carbon porosity.

H_2 shows the largest diffusivity enhancement with filler loading. Its small kinetic size makes this trend consistent with access to the smallest available pathways in the biochar–polymer microstructure. However, the fast uptake kinetics produce comparatively large uncertainties, and the data do not justify describing the carbon phase as a continuous low-resistance channel.

In contrast, the 5 wt% membrane shows markedly lower N_2 diffusivity across the investigated pressure range. Because a single, uniform densification mechanism would not also explain the increases in CO_2, CH_4, and H_2 diffusivity, the N_2 result is better described as gas-specific: weak N_2 affinity, restricted access to ultramicropores, and increased path tortuosity may act together. This interpretation is consistent with the data but remains tentative without direct free-volume or segmental-mobility measurements.

Overall, the D trends reveal gas-dependent effects rather than a uniform mobility change. CO_2, CH_4, and H_2 benefit from biochar-associated interfacial or porous transport to different extents, whereas N_2 is strongly hindered at 5 wt%. Together with the S data, these trends explain the separation performance without requiring FESEM-based claims of chain rigidification or denser packing.

3.2.1.3. Gas permeability. The combined effect of sorption and diffusion

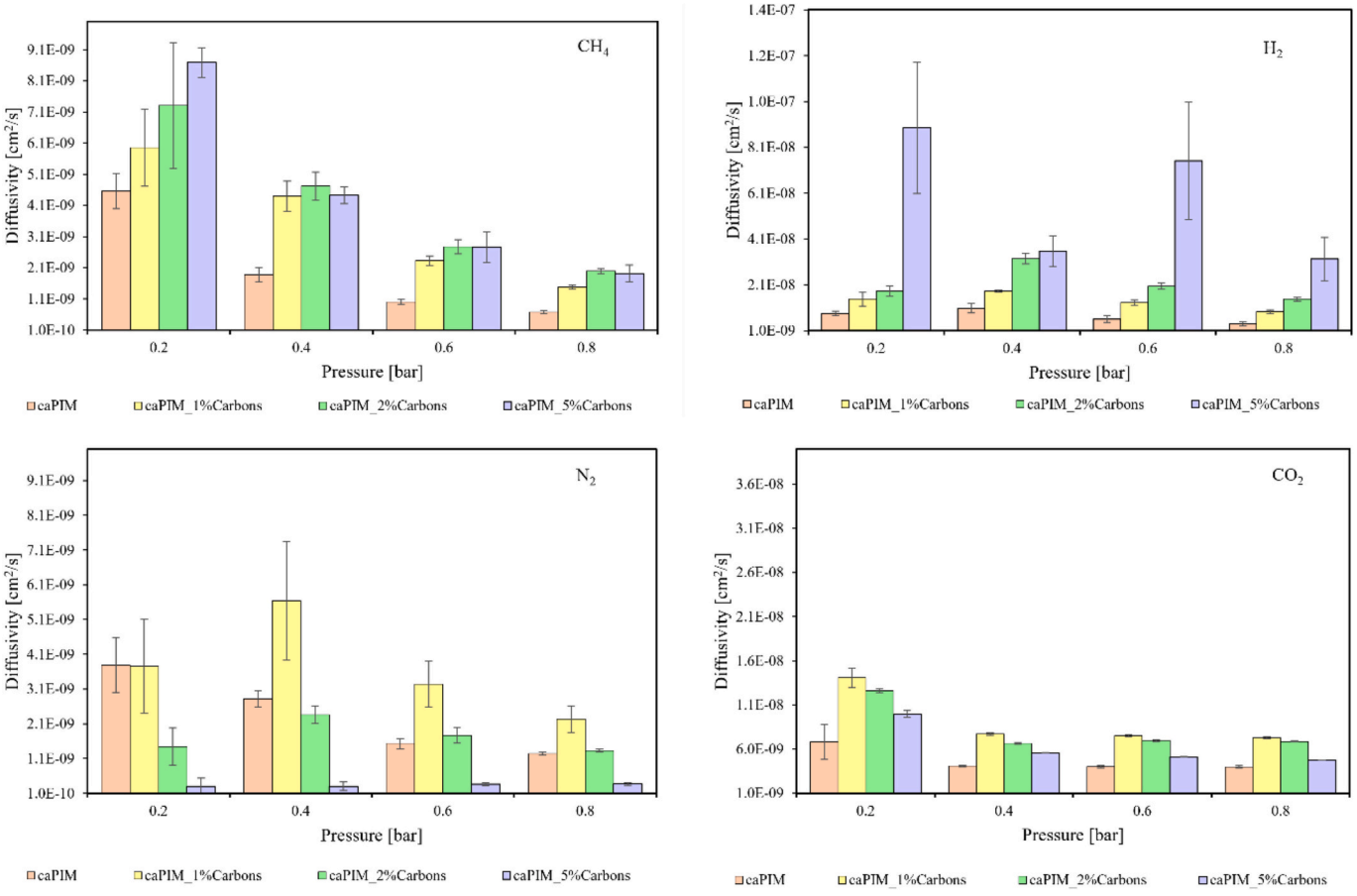


Fig. 7. Diffusivity coefficients of CH_4, H_2, N_2, and CO_2 in caPIM and caPIM-based mixed matrix membranes containing 1, 2, and 5 wt% carbon filler, plotted as a function of gas partial pressure. Error bars represent the standard error calculated from replicate measurements performed at the same pressure.

is reflected in the permeability coefficients summarized in Fig. 8. As expected from the product $P = S{\cdot}D$, permeability trends largely mirror the interplay between solubility and diffusivity discussed above.

For CO_2, pristine caPIM exhibits permeabilities of 11 Barrer at 0.2 bar, decreasing to 4.7 Barrer at 0.8 bar. All carbon-containing membranes show higher CO_2 permeabilities than the neat polymer over the entire pressure range. At 0.4 bar, P_{CO_2} increases from 5.8 Barrer in caPIM to 8.2–9.5 Barrer in the membranes containing 1–5 wt% carbon, while at 0.2 bar the caPIM_5% membrane reaches approximately 20.9 Barrer, nearly doubling the permeability of the pristine polymer. This enhancement arises from the combined contribution of increased CO_2 diffusivity (particularly at 1–2 wt%) and increased solubility (most pronounced at 5 wt%), confirming the favorable role of the carbon filler in facilitating CO_2 transport through the coupled polymer–carbon network.

Hydrogen permeability is even more strongly affected by carbon incorporation. In caPIM, P_{H_2} decreases from 33 Barrer at 0.2 bar to 14 Barrer at 0.8 bar. The introduction of carbon leads to a dramatic permeability enhancement, which becomes more pronounced with increasing loading. At 0.4 bar, hydrogen permeability increases to approximately 112 Barrer (1 wt%), 143 Barrer (2 wt%), and 151 Barrer (5 wt%), while at 0.6 bar the 5 wt% membrane reaches about 310 Barrer, more than an order of magnitude higher than caPIM. Although the associated error bars are relatively large due to the fast uptake kinetics of hydrogen, the trend is robust and clearly indicates that carbon incorporation strongly facilitates H_2 permeation. This behavior is consistent with the combined effects of enhanced diffusivity and the ability of hydrogen to efficiently access the ultramicroporous domains of the carbon filler, which provide low-resistance, highly connected transport pathways.

For methane, the effect of carbon incorporation is more moderate. In caPIM, P_{CH_4} decreases from 5.8 Barrer at 0.2 bar to 0.5 Barrer at 0.8 bar. Carbon-loaded membranes exhibit permeabilities comparable to or moderately higher than those of the pristine polymer, particularly at intermediate and high pressures. At 0.6 bar, methane permeability increases from 0.86 Barrer in caPIM to 1.2–1.8 Barrer in the carbon-containing membranes, while at 0.8 bar the permeabilities of the 2 wt % and 5 wt% membranes are approximately twice that of the neat polymer. Since CH_4 solubility is not enhanced by carbon addition, these permeability gains primarily reflect the diffusivity enhancement induced by microstructural reorganization and partial utilization of the carbon microporosity.

In contrast, nitrogen permeability is systematically reduced upon carbon incorporation. Pristine caPIM exhibits P_{N_2} values of 2.6 Barrer at 0.2 bar and 0.5 Barrer at 0.8 bar. With carbon addition, permeabilities decrease markedly, particularly at higher loadings. At 0.2 bar, P_{N_2} drops from 2.6 Barrer in caPIM to 0.6 Barrer for the 2 wt% membrane and to 0.3 Barrer for the 5 wt% membrane, while at 0.8 bar the 2–5 wt% membranes display permeabilities around 0.2–0.3 Barrer, less than half that of the pristine polymer. This behavior reflects the combined decrease in both N_2 solubility and diffusivity and indicates that nitrogen molecules, which have a larger kinetic diameter and weak affinity for the carbon phase, are selectively hindered by increased path tortuosity; carbon-induced densification is a plausible contributor but is not asserted, as it was not measured independently.

Overall, the permeability data confirm that carbon incorporation transforms caPIM into a membrane platform combining high permeability and high selectivity through a balanced interplay of sorption,

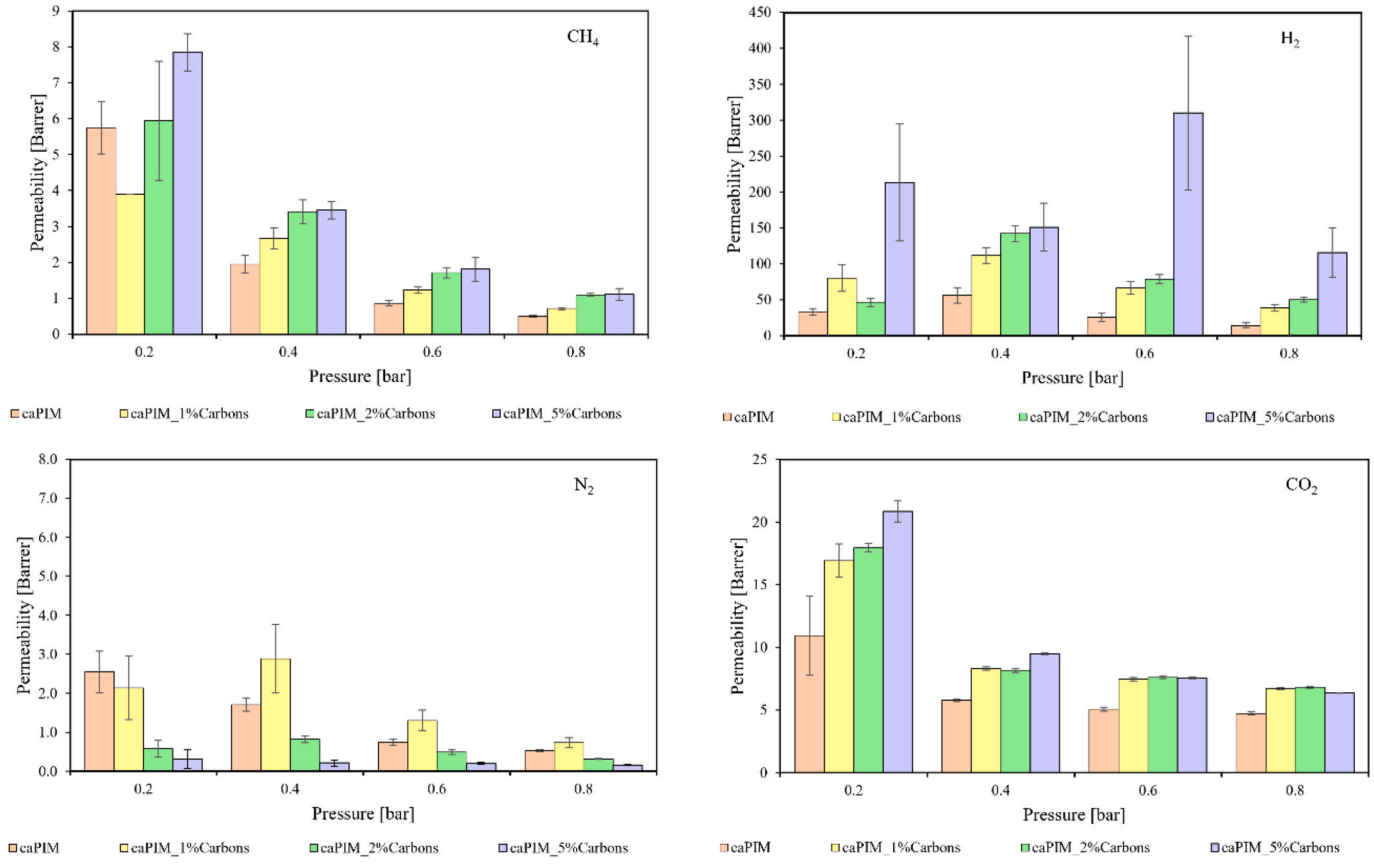


Fig. 8. Permeability coefficients of CH_4, H_2, N_2, and CO_2 in caPIM and caPIM-based mixed matrix membranes with different carbon loadings (1, 2, and 5 wt%), plotted as a function of gas partial pressure. Error bars represent the propagated standard error obtained from the standard errors of the solubility and diffusion coefficients.

diffusivity, and filler–polymer interaction. According to recent conceptual frameworks for MMMs design, such behavior is characteristic of systems where the filler provides accessible porosity and selective transport pathways without introducing interfacial defects.

The addition of pristine PIM-1 to Fig. 8 provides a useful benchmark for interpreting the permeability trends. As expected, PIM-1 exhibits very high permeability for CO_2, CH_4, and N_2 due to its high intrinsic free volume and correspondingly high gas diffusivity. In particular, CO_2 permeability in pristine PIM-1 decreases from approximately 306 Barrer at 0.2 bar to 75 Barrer at 0.8 bar, values significantly higher than those of caPIM and caPIM/carbon membranes. However, this high permeability is not selective, since N_2 permeability is also high, ranging from approximately 48 to 9 Barrer over the same pressure range.

In contrast, caPIM_5%carbons exhibits lower absolute CO_2 permeability than pristine PIM-1, but it strongly suppresses N_2 permeability, which remains close to 0.2–0.3 Barrer. This selective reduction of N_2 transport is the key factor responsible for the enhanced CO_2/N_2 and H_2/N_2 separation performance of the carbon-containing caPIM membranes. Therefore, the comparison with PIM-1 clarifies that the advantage of the caPIM/carbon mixed matrix membranes is not simply related to maximizing permeability, but rather to achieving a more favorable balance between permeability and selectivity.

This balance directly reflects the trade-off associated with the choice of caPIM: hydrolysis reduces CO_2 permeability relative to PIM-1 (~306 → ~11 Barrer), consistent with literature reports of reduced chain spacing and redistributed free volume in hydrolyzed PIM-1, [37] while the resulting ideal CO_2/N_2 selectivity of the caPIM/5 wt% biochar membrane ($\alpha \approx 67$) is substantially higher than achievable with unmodified PIM-1, justifying this compromise for applications where selectivity and product purity are prioritized over raw permeability.

For H_2, the effect is particularly relevant. While pristine PIM-1 shows H_2 permeability values ranging from approximately 117 to 39 Barrer, caPIM_5%carbons reaches significantly higher values, from approximately 214 Barrer at 0.2 bar to 116 Barrer at 0.8 bar. This confirms that the incorporation of the N-doped carbon filler promotes H_2 transport, most likely through a coupled polymer–carbon diffusion mechanism,

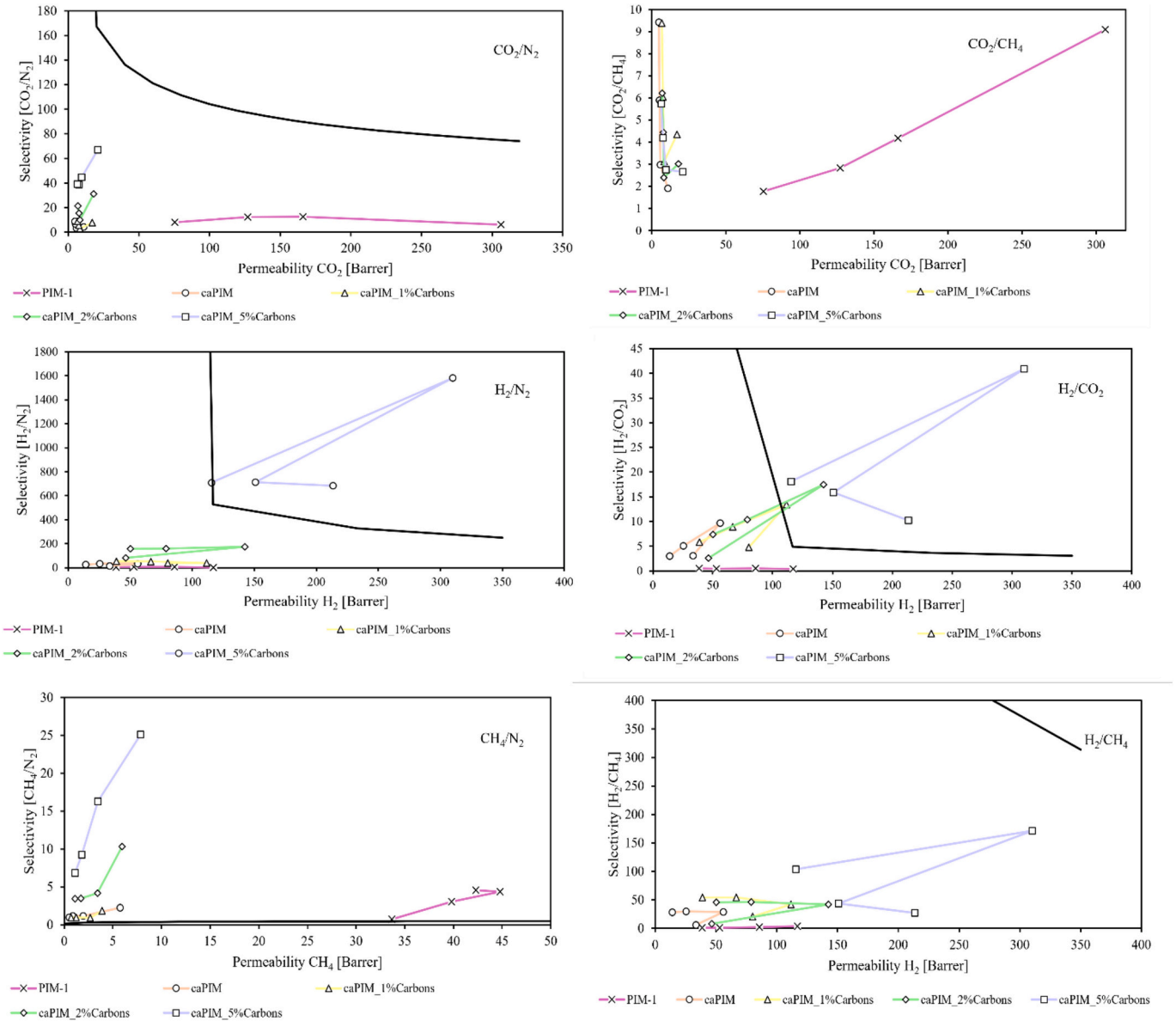


Fig. 9. Permeability–selectivity trade-off plots for CO_2/N_2, CO_2/CH_4, CH_4/N_2, H_2/N_2, H_2/CH_4, and H_2/CO_2 gas pairs. The experimentally measured PIM-1 membrane was included as a reference. Updated Robeson-type upper-bound relationships were used where available: the 2015 upper bounds [38] for H_2/N_2 and H_2/CH_4, and the 2019 upper bounds [39] for CO_2/N_2 and CO_2/CH_4.

while simultaneously maintaining strong N_2 rejection.

3.2.1.4. Permeability-selectivity trade-off. To further assess separation performance, ideal selectivity was plotted as a function of the permeability of the more permeable gas in each pair and compared with Robeson's upper bound, as shown in Fig. 9. [24,38]

For H_2/CO_2 and CH_4/N_2, the original Robeson 2008 upper bounds [24] were retained, as no more recent generally accepted coefficients were identified.

For CO_2/N_2, the caPIM_5%carbons membrane occupies a highly selective region of the trade-off plot. Although its CO_2 permeability remains lower than that of pristine PIM-1, the strong suppression of N_2 permeability shifts the membrane toward a more favorable CO_2/N_2 separation balance. This indicates that the main advantage of carbon incorporation is not simply an increase in CO_2 permeability, but the selective reduction of N_2 transport.

In contrast, for the CO_2/CH_4 pair, carbon incorporation does not lead to a comparable improvement. Although CO_2 permeability increases, the simultaneous increase in CH_4 diffusivity limits selectivity gains, and all membranes remain below the Robeson upper bound for this gas pair.

The CH_4/N_2 pair exhibits an atypical transport behavior, as methane permeability exceeds that of nitrogen in all biochar-based mixed matrix membranes (Table S3). Unlike conventional glassy polymers, where gas transport is mainly governed by molecular size discrimination and N_2 permeability is typically comparable to or higher than CH_4, the present membranes show enhanced CH_4 transport arising from the combined contribution of higher methane diffusivity and higher methane solubility.

In particular, the incorporation of the carbon-based filler appears to promote preferential CH_4–filler interactions[37], enhancing methane mobility while simultaneously suppressing N_2 diffusion, especially at higher filler loading. As a consequence, the apparent position above the Robeson upper bound does not necessarily indicate extraordinary separation performance, but rather reflects a reversed transport regime in which both diffusivity and sorption selectively favor CH_4 over N_2 (Tables S1–S2).

For H_2/N_2, the caPIM_5%carbons membrane shows the most pronounced improvement. Compared with pristine PIM-1, the carbon-containing membrane combines high H_2 permeability with a much stronger reduction in N_2 permeability (Table S3), resulting in markedly enhanced H_2/N_2 selectivity. Its position relative to the updated 2015 upper bound highlights the ability of the caPIM/carbon system to move toward a high-selectivity regime through selective N_2 rejection while maintaining relevant H_2 transport.

For the H_2/CO_2 pair, selectivity also increases with carbon loading, particularly at 5 wt%, where the membranes approach or exceed the Robeson upper bound at all pressures, the dominant contribution arising from the strong enhancement of hydrogen diffusivity relative to the other gases (Table S2). For H_2/CH_4, although selectivity likewise increases with carbon loading, all membranes remain below the corresponding upper bound, which lies at considerably higher selectivity values for this gas pair.

It should be noted that the caPIM_5%carbons membrane shows a relatively large uncertainty in H_2 permeability, particularly at 0.2 bar, and these selectivity values should therefore be interpreted with caution.

To verify that the above conclusions are not driven by the nominal selectivity values, the trade-off plots were reconstructed using a worst-case criterion, in which each data point was repositioned according to the lower bound of its selectivity (nominal value minus the associated uncertainty, Tables S3–S4); the resulting plots are reported in Fig. S9.

For the large majority of the data points the position relative to the upper bound is essentially preserved, confirming that the performance assessment holds also under the most conservative estimate compatible with the experimental uncertainty. In particular, for the H_2/CO_2 gas pair the membrane remains above the upper bound at all the investigated pressures, while for H_2/N_2 it lies above the upper bound at 0.6 bar and close to it at the other pressures. All caPIM membranes also remain above the upper bound for CH_4/N_2 even in the worst-case estimate, although, as discussed above, this reflects the reversed transport regime rather than an exceptional separation performance.

The largest deviations occur, as expected, for those points where the low uptake of the less permeable gas approaches the sensitivity limit of the gravimetric method (Section 2.7). The analysis therefore confirms that the enhanced separation performance of the carbonised membranes is a robust feature rather than an artefact of the measurement uncertainty.

Overall, carbon incorporation systematically shifts caPIM membranes toward enhanced separation performance for gas pairs dominated by diffusivity contrast (H_2-containing pairs) or by selective restriction of N_2 transport. Among the investigated compositions, the membrane containing 5 wt% carbon consistently achieves the most pronounced improvements, positioning this system as a promising candidate for high-flux and highly selective gas separation applications. This behavior aligns with recent literature showing that MMMs designed with intrinsically compatible fillers and controlled interfacial interactions are among the few systems capable of simultaneously achieving high permeability and high selectivity beyond the Robeson upper bound.

3.2.1.5. Comparison with state-of-the-art. The performance of the caPIM membranes incorporating 5 wt% mesoporous carbons developed in this work was benchmarked against state-of-the-art systems reported in the recent literature (Table 1).

The PIM-1 reference values reported for comparison are higher than those obtained in our study, as that PIM-1 sample was subjected to methanol treatment, which may induce partial regeneration of the free-volume fraction, thereby mitigating aging effects and temporarily enhancing gas transport properties. [44]

The caPIM/5% mesoporous carbon membranes exhibit a hydrogen permeability of 214 Barrer and H_2/N_2 selectivity of 684 at 0.2 bar, reaching 1581 at 0.6 bar and remaining close to or above 700 over the whole pressure range investigated (Table 1), values being remarkably superior to all reference membranes examined in this study. This exceptional selectivity can be attributed to the synergistic effect between the intrinsic microporosity of the carboxylated caPIM matrix and the controlled mesoporosity of the carbon additives, which introduces a more efficient molecular sieving mechanism compared to unmodified PIMs.

Notably, Matrimid-based membranes, both in the carbon nanofiber configuration (α $H_2/N_2 = 67.5$) and in the ternary blend with PMMA and graphene oxide (α $CO_2/N_2 = 729.7$), exhibit high selectivities but at the expense of significantly lower permeabilities. The PIM-TB-PI system, incorporating biphenyl units and Tröger's base, displays intermediate performance (α $H_2/N_2 = 42.3$) with modest hydrogen permeability (52 Barrer).

The primary advantage of the caPIM/mesoporous carbon membranes lies in the optimal balance between selectivity and permeability, positioning them favourably with respect to the Robeson upper bound for the H_2/N_2 gas pair. The carboxylic functionalization of the PIM-1 matrix, combined with the incorporation of 5 wt% mesoporous carbons, enables the membrane.

to transcend the typical permeability-selectivity trade-off that constrains the performance of conventional polymeric membranes.

4. Conclusions

Chitosan-derived N-doped biochar modifies caPIM transport through distinct sorption and diffusion contributions. At 5 wt% filler and 0.2 bar, CO_2 permeability increases from 11 to approximately 21 Barrer relative

Table 1
Comparison table of the gas separation performance of the membrane caPIM +5% with representative state-of-the-art membranes from the literature.(*), (†), (‡)

Membrane type / reference	Material / structure	Test conditions (P, T)	PH_2 (Barrer)	PN_2* (Barrer)	PCO_2 (Barrer)	PCH_4 (Barrer)	$\alpha(H_2/N_2)^{\dagger}$	$\alpha(CO_2/N_2)^{\ddagger}$
caPIM + 5% mesoporous carbons‡	PIM-1 carboxylate + mesoporous carbons	0.2–0.8 bar 40 °C	0.2 bar =214	0.2 bar =0.312	0.2 bar = 21	0.2 bar =7.8	0.2 bar =684	0.2 bar = 67
			0.4 bar =151	0.4 bar =0.212	0.4 bar =9.5	0.4 bar =3.5	0.4 bar =712	0.4 bar =45
			0.6 bar =310	0.6 bar =0.196	0.6 bar =7.6	0.6 bar =1.8	0.6 bar =1581	0.6 bar =39
			0.8 bar =116	0.8 bar =0.163	0.8 bar =6.4	0.8 bar =1.1	0.8 bar =709	0.8 bar =39
PIM-BTrip [39]	PIM derived from a benzotriptycene monomer	1 bar, 25 °C	9430	339	9200	412	27.8	27.1
PIM-TB-PI [40]	Polyimides containing biphenyl and Tröger's base	2 bar, 35 °C	52.1	1.23	30.7	0.80	42.3	25.0
Matrimid/CNF4 [41]	Matrimid + carbon nanofibers (CNFs)	20 atm upstream, 1 atm downstream, 35 °C	16.4	0.24	9.3	0.1	67.5	38.8
AO-PIM-1/UiO-66(Zr) [42]	Amine-oxidized PIM-1 + MOF	2 bar, 35 °C	1068.9	50.9	205.7	55.3	21	4
PMMA/10%Matrimid/ 2%GO [43]	Polymethyl methacrylate + Matrimid + graphene oxide	10 bar, 35 °C	–	0.0195	14.23	0.0165	–	729.7
PIM-1[40]	PIM-1 membrane	3.5 atm, 35 °C	2918	192	3825	268	15.2	19.9

* For the caPIM + 5% carbons membrane, N_2 permeability values are reported with additional decimal places owing to their low magnitude, so that the derived selectivity values can be reproduced from the tabulated data with minimal rounding-induced deviation.

† For the caPIM + 5% carbons membrane, selectivity values were calculated from the non-rounded permeability data; minor discrepancies may therefore arise if they are recalculated from the rounded permeability values reported in the table.

‡ For the caPIM + 5% carbons membrane, the associated uncertainties (standard errors) for each reported value are provided in Tables S3 and S4 (Supporting Information).

to neat caPIM, while N_2 permeability falls from 2.6 to about 0.3 Barrer, yielding an ideal CO_2/N_2 selectivity near 67. The selectivity gain therefore arises mainly from N_2 rejection; CO_2 permeability remains substantially below the 306 Barrer measured for PIM-1.

For H_2/N_2, the same membrane combines an H_2 permeability of approximately 214 Barrer with very low N_2 permeability, producing ideal selectivities in the 10^2–10^3 range across the tested pressures. The resolved S and D data show that CO_2 benefits from enhanced sorption at 5 wt%, H_2 primarily from faster diffusion, and N_2 is hindered in both contributions. These gas-dependent trends are consistent with competing interfacial, ultramicropore-access, and tortuosity effects rather than a uniform change in polymer packing.

The study demonstrates the specific value of pairing a polar, microwave-hydrolyzed PIM matrix with low loadings of waste-derived N-doped biochar. Its main limitation is that the results are based on pure gases and do not include direct measurements of segmental mobility or in-membrane free volume; mixed-gas testing and thin-film permeance measurements are therefore required before process-level conclusions can be drawn.

These findings support the use of intrinsically compatible, waste-derived biochar as a sustainable filler for high-performance MMMs, in line with current design principles for defect-free, selective mixed matrix membranes.

Declaration of competing interest

The authors declare that they have no known competing financial interests or personal relationships that could have appeared to influence the work reported in this paper.

Acknowledgments

This article was partially funded under the National Recovery and Resilience Plan (NRRP), Mission 4 “Education and Research”—Component 2 “From research to business”—Investment.

3.1 “Fund for the realization of an integrated system of research and innovation infrastructures”—Call for tender No. n. 3264 of 28/12/2021 of Italian Ministry of Research funded by the European Union—NextGenerationEU—Project code: IR0000027, Concession Decree No. 128 of 21/06/2022 adopted by the Italian Ministry of Research, CUP: B33C22000710006, Project title: iENTRANCE.

This study was carried out within the Agritech National Research Center and received funding from the European Union NextGenerationEU (PIANO NAZIONALE DI RIPRESA E RESILIENZA (PNRR) – MISSIONE 4 COMPONENTE 2, INVESTIMENTO 1.4 – D.D. 1032.

June 17, 2022, CN00000022). Furthermore, authors wish to thank European Union for the financial support through the Next Generation EU- projects “Nord Ovest Digitale E Sostenibile- NODES” (PNRR, D.D. n.1054 June 23, 2022), NEST “Network for Energy Sustainable Transition- NEST”(PE0000021, D.D. n.341 March 15, 2022) and PNRR Mission 4 “Education and Research”—Component 2 “From research to business”—Investment 3.1 “Fund for the realization of an integrated system of research and innovation infrastructures”—Call for tender No. n. 3264 of 28/12/2021 of Italian Ministry of Research funded by the European Union—NextGenerationEU—Project code: IR0000027, Concession Decree No. 128 of 21/06/2022 adopted by the Italian Ministry of Research, CUP: B33C22000710006, Project title: iENTRANCE. Authors also acknowledge Ministero dello Sviluppo Economico (MISE) and Ministero della Transizione Ecologica (MITE) for the financial support. This manuscript reflects only the authors' views and opinions, neither the European Union nor the European Commission can be considered responsible for them.

M.A.O.L. acknowledge FCT for the Researcher position (CEECIND/01158/2021), the funding from the European Union's Horizon Europe research and innovation programme (ERA-PF grant agreement No 101090287) and FCT/MCTES, I.P., through national funds (PIDDAC), co-financed by the European Regional Development Fund (ERDF) of the

European Union, through the FEDER program and national funds related to operation no. 16589 (operation code: COMPETE2030-FEDER-00776600) of Portugal 2030 (CharM project). This work was developed within the scope of the project CICECO–Aveiro Institute of Materials, UID/50011 & LA/P/0006/2020 (DOI 10.54499/LA/P/0006/2020), financed by national funds through the FCT/MCTES (PIDDAC).

Appendix A. Supplementary data

Supplementary data to this article can be found online at https://doi.org/10.1016/j.seppur.2026.140717.

Data availability

The research data supporting this article are available in Zenodo under DOI: 10.5281/zenodo.21034883

References

[1] A.N. Shafawi, A.R. Mohamed, P. Lahijani, M. Mohammadi, Recent advances in developing engineered biochar for CO2 capture: an insight into the biochar modification approaches, J. Environ. Chem. Eng. 9 (2021), https://doi.org/10.1016/j.jece.2021.106869.
[2] X. Wang, C. Song, Carbon capture from flue gas and the atmosphere: a perspective, Front. Energy Res. 8 (2020), https://doi.org/10.3389/fenrg.2020.560849.
[3] I. Correia, M. Ilkaeva, M. Castellino, S. Bocchini, R.M. Novais, L. Mafra, N. P. Goncalves, M.A. Lourenco, Impact of pyrolysis heating methods on biochars with enhanced CO2/N2 separation and their incorporation in 3D-printed composites, J. Environ. Chem. Eng. 12 (2024), https://doi.org/10.1016/j.jece.2024.113875.
[4] A.I. Osman, M. Hefny, M.I.A. Abdel Maksoud, A.M. Elgarahy, D.W. Rooney, Recent advances in carbon capture storage and utilisation technologies: a review, Environ. Chem. Lett. 19 (2021) 797–849, https://doi.org/10.1007/s10311-020-01133-3.
[5] Y. Qiao, C. Wu, Nitrogen enriched biochar used as CO2 adsorbents: a brief review, Carbon Capture Sci. Technol. 2 (2022), https://doi.org/10.1016/j.ccst.2021.100018.
[6] H. Zhang, Z. Yu, Q. Huang, A review: utilization of biochar for wastewater treatment, in: Application of Adsorbents for Water Pollution Control, 2012, pp. 413–431.
[7] M.A. Lourenço, T. Frade, M. Bordonhos, M. Castellino, M.L. Pinto, S. Bocchini, N-doped sponge-like biochar: a promising CO_2 sorbent for CO_2/CH_4 and CO_2/N_2 gas separation, Chem. Eng. J. 470 (2023), https://doi.org/10.1016/j.cej.2023.144005.
[8] J.W. Jeon, D.-G. Kim, E. Sohn, Y. Yoo, Y.S. Kim, B.G. Kim, J.-C. Lee, Highly carboxylate-functionalized polymers of intrinsic microporosity for CO_2-selective polymer membranes, Macromolecules 50 (2017) 8019–8027, https://doi.org/10.1021/acs.macromol.7b01332.
[9] P.M. Budd, E.S. Elabas, B.S. Ghanem, S. Makhseed, N.B. McKeown, K.J. Msayib, C. E. Tattershall, D. Wang, Solution-processed, organophilic membrane derived from a polymer of intrinsic microporosity, Adv. Mater. 16 (2004) 456–459, https://doi.org/10.1002/adma.200306053.
[10] P.M. Budd, N.B. McKeown, B.S. Ghanem, K.J. Msayib, D. Fritsch, L. Starannikova, N. Belov, O. Sanfirova, Y. Yampolskii, V. Shantarovich, Gas permeation parameters and other physicochemical properties of a polymer of intrinsic microporosity: Polybenzodioxane PIM-1, J. Membr. Sci. 325 (2008) 851–860.
[11] G. Bengtson, S. Neumann, V. Filiz, Membranes of polymers of intrinsic microporosity (PIM-1) modified by poly (ethylene glycol), Membranes 7 (2017) 28, https://doi.org/10.3390/membranes7020028.
[12] D. Lin-Vien, N.B. Colthup, W.G. Fateley, J.G. Grasselli, The Handbook of Infrared and Raman Characteristic Frequencies of Organic Molecules, Elsevier, 1991.
[13] T.J. Zimudzi, K.E. Feldman, J.F. Sturnfield, A. Roy, M.A. Hickner, C.M. Stafford, Quantifying carboxylic acid concentration in model polyamide desalination membranes via Fourier transform infrared spectroscopy, Macromolecules 51 (2018) 6623–6629, https://doi.org/10.1021/acs.macromol.8b01194.
[14] G. (George) Socrates, Chapter 4. Triple Bond Compounds, in: Infrared Characteristic Group Frequencies : Tables and Charts, Third edition, John Wiley & Sons, Ltd, New York, U.S., 2001, p. 84. https://cir.nii.ac.jp/crid/1130282272591531904. accessed May 3, 2024.
[15] C.R. Mason, L. Maynard-Atem, K.W.J. Heard, B. Satilmis, P.M. Budd, K. Friess, M. Lanč, P. Bernardo, G. Clarizia, J.C. Jansen, Enhancement of CO_2 affinity in a polymer of intrinsic microporosity by amine modification, Macromolecules 47 (2014) 1021–1029, https://doi.org/10.1021/ma401869p.
[16] N. Du, G.P. Robertson, J. Song, I. Pinnau, M.D. Guiver, High-performance Carboxylated polymers of intrinsic microporosity (PIMs) with Tunable gas transport properties, Macromolecules 42 (2009) 6038–6043, https://doi.org/10.1021/ma9009017.
[17] National Institute of Standards and Technology, 2-pyrrolidinone, 1-methyl-, NIST chemistry WebBook, SRD 69. https://webbook.nist.gov/cgi/cbook.cgi?ID=C872504&Units=SI&Mask=80#IR-Spec, 2026 (accessed September 3, 2025).
[18] National Institute of Standards and Technology, carbon dioxide, NIST chemistry WebBook, SRD 69. https://webbook.nist.gov/cgi/cbook.cgi?ID=C124389&Units=SI&Type=IR-SPEC&Index=1#IR-SPEC, 2026 (accessed September 3, 2025).
[19] H.-H. Tseng, P.-T. Shiu, Y.-S. Lin, Effect of mesoporous silica modification on the structure of hybrid carbon membrane for hydrogen separation, Int. J. Hydrog. Energy 36 (2011) 15352–15363, https://doi.org/10.1016/j.ijhydene.2011.08.060.
[20] C.N. Brysch, E. Wold, M. Patterson, R.O. Olivares, J.F. Eberth, F.R. Hernandez, Chitosan and chitosan composites reinforced with carbon nanostructures, J. Alloys Compd. 615 (2014) S515–S521.
[21] M. Nakamizo, H. Honda, M. Inagaki, Raman spectra of ground natural graphite, Carbon 16 (1978) 281–283.
[22] B. Smith, The Infrared Spectra of Polymers, VI: Polymers with CO bonds. https://www.spectroscopyonline.com/view/the-infrared-spectra-of-polymers-vi-polymers-with-c-o-bonds, 2022 (accessed December 9, 2025).
[23] Y. Peng, Z. Xia, Y. Song, Y. Zhang, Y. Li, P. Zhang, Highly carboxylic acid functionalized PIM-1 by hydrothermal method: mechanistic study of gas separation properties, Nano Select 3 (2022) 1395–1406, https://doi.org/10.1002/nano.202200082.
[24] L.M. Robeson, The upper bound revisited, J. Membr. Sci. 320 (2008) 390–400.
[25] C. Astorino, E. De Nardo, G. Giordano, G. Ferraro, F. Cardano, S. Lettieri, M. Bartoli, A. Fin, L. Goldoni, F. De Boni, M.E. Tresso, C.F. Pirri, S. Bocchini, Optimized Hydrolysis of Polymers with Intrinsic Microporosity (PIM-1): Fast Microwave-Assisted Synthesis of Carboxylated PIMs, 2026.
[26] A. Jha, N. Gupta, S. Divekar, S. Dasgupta, V.C.S. Palla, R.S. Murali, Fabrication of high-performance biochar incorporated Pebax® 1657 membranes for CO2 separation, Process. Saf. Environ. Prot. 188 (2024) 204–216.
[27] Z. Tian, D. Li, W. Zheng, Q. Chang, Y. Sang, F. Lai, J. Wang, Y. Zhang, T. Liu, M. Antonietti, Heteroatom-doped noble carbon-tailored mixed matrix membranes with ultrapermeability for efficient CO2 separation, Mater. Horiz. 10 (2023) 3660–3667.
[28] F. Weigelt, P. Georgopanos, S. Shishatskiy, V. Filiz, T. Brinkmann, V. Abetz, Development and characterization of defect-free Matrimid® mixed-matrix membranes containing activated carbon particles for gas separation, Polymers 10 (2018) 51.
[29] Md.R. Hasan, J. Coronas, How can the filler-polymer interaction in mixed matrix membranes be enhanced? ChemPlusChem 89 (2024) e202400456 https://doi.org/10.1002/cplu.202400456.
[30] J. Crank, The Mathematics of Diffusion, Oxford University Press, 1975.
[31] G. Socrates, Infrared and Raman Characteristic Group Frequencies: Tables and Charts, Third edition, John Wiley & Sons, New York, U.S., 2004.
[32] M. Giorcelli, M. Bartoli, Development of coffee biochar filler for the production of electrical conductive reinforced plastic, Polymers 11 (2019) 1916, https://doi.org/10.3390/polym11121916.
[33] Y. Ma, S. Velioğlu, Z. Yin, R. Wang, J.W. Chew, Molecular dynamics investigation of membrane fouling in organic solvents, J. Membr. Sci. 632 (2021) 119329.
[34] M.R. Abdul Hamid, Y. Qian, R. Wei, Z. Li, Y. Pan, Z. Lai, H.-K. Jeong, Polycrystalline metal-organic framework (MOF) membranes for molecular separations: engineering prospects and challenges, J. Membr. Sci. 640 (2021) 119802, https://doi.org/10.1016/j.memsci.2021.119802.
[35] F. Tuinstra, J.L. Koenig, Raman spectrum of graphite, J. Chem. Phys. 53 (1970) 1126–1130.
[36] Y. Rong, M.J. Large, M. Tripathi, S.P. Ogilvie, A. Amorim Graf, B. Mao, J. Tunesi, J. P. Salvage, A.A.K. King, A. Pasquazi, M. Peccianti, R. Malpass-Evans, N. B. McKeown, F. Marken, A.B. Dalton, Charge transfer hybrids of graphene oxide and the intrinsically microporous polymer PIM-1, ACS Appl. Mater. Interfaces 11 (2019) 31191–31199, https://doi.org/10.1021/acsami.9b09832.
[37] M. Hu, J. Liu, J. Kong, P. Jia, N. Qi, Y. Wu, Z. Chen, S. Xu, N. Li, Free volume and gas transport properties of hydrolyzed polymer of intrinsic microporosity (PIM-1) membrane studied by positron annihilation spectroscopy, Microporous Mesoporous Mater. 335 (2022) 111770.
[38] R. Swaidan, B. Ghanem, I. Pinnau, Fine-tuned intrinsically Ultramicroporous polymers redefine the permeability/selectivity upper bounds of membrane-based air and hydrogen separations, ACS Macro Lett. 4 (2015) 947–951, https://doi.org/10.1021/acsmacrolett.5b00512.
[39] B. Comesaña-Gándara, J. Chen, C.G. Bezzu, M. Carta, I. Rose, M.-C. Ferrari, E. Esposito, A. Fuoco, J.C. Jansen, N.B. McKeown, Redefining the Robeson upper bounds for CO_2/CH_4 and CO_2/N_2 separations using a series of ultrapermeable benzotriptycene-based polymers of intrinsic microporosity, Energy Environ. Sci. 12 (2019) 2733–2740.
[40] A. Rodríguez, M.V. Velázquez Tundidor, Y. Cruz, F.E. Rodríguez-González, M. J. Aguilar-Vega, R. Sulub-Sulub, S. Ravula, J.E. Bara, C.A. Terraza, A. Tundidor-Camba, Polyimides containing biphenyl and Tröger's base units for gas separation membranes, ACS Appl. Polym. Mater. 6 (2024) 3342–3353, https://doi.org/10.1021/acsapm.3c03193.
[41] M. Dohade, Incorporation of carbon nanofibers into a Matrimid polymer matrix: effects on the gas permeability and selectivity properties, J. Appl. Polym. Sci. 135 (2018) 46019, https://doi.org/10.1002/app.46019.
[42] I.-D. Carja, S.R. Tavares, O. Shekhah, A. Ozcan, R. Semino, V.S. Kale, M. Eddaoudi, G. Maurin, Insights into the enhancement of MOF/polymer adhesion in mixed-matrix membranes *via* polymer functionalization, ACS Appl. Mater. Interfaces 13 (2021) 29041–29047, https://doi.org/10.1021/acsami.1c03859.
[43] A. Salehi, M. Omidkhah, A.E. Amooghin, M.M.M. Sharifzadeh, Improved gas separation performance of PMMA/Matrimid@ 5218/graphene oxide (GO) mixed matrix membranes, J. CO_2 Util. 91 (2025) 103012.
[44] W.F. Yong, F.Y. Li, T.-S. Chung, Y.W. Tong, Highly permeable chemically modified PIM-1/Matrimid membranes for green hydrogen purification, J. Mater. Chem. A 1 (2013) 13914–13925.